ROYAL SOCIETY
OF CHEMISTRY

PAPER

Check for updates

Atomic-scale investigation of the reversible α- to ω-phase lithium ion charge − discharge characteristics of electrodeposited vanadium pentoxide nanobelts†

Haytham E. M. Hussein, [ID] *[a] Richard Beanland, [ID] *[b] Ana M. Sànchez, [ID] [b] David Walker, [ID] [a] Marc Walker, [ID] [b] Yisong Han [ID] [b] and Julie V. Macpherson [ID] *[a]

Using an electrochemical potential pulse methodology in a mixed solvent system, electrochemical deposition of amorphous vanadium pentoxide (V_2O_5) nanobelts is possible. Crystallisation of the material is achieved using in air annealing with the temperature of crystallisation identified using *in situ* heating transmission electron microscopy (TEM). The resulting α-phase V_2O_5 nanobelts have typical thicknesses of 10−20 nm, widths and lengths in the range 5−37 nm (mean 9 nm) and 15−221 nm (mean 134 nm), respectively. One-cycle reversibility studies for lithium intercalation (discharge) and de-intercalation (charge) reveal a maximum specific capacity associated with three lithium ions incorporated per unit cell, indicative of ω-$Li_3V_2O_5$ formation. Aberration corrected scanning TEM confirm the formation of ω-$Li_3V_2O_5$ across the entirety of a nanobelt during discharge and also the reversible formation of the α-V_2O_5 phase upon full charge. Preliminary second cycle studies reveal reformation of the ω-$Li_3V_2O_5$, accompanied with a morphological change in the nanobelt dimensions. Achieving α-V_2O_5 to ω-$Li_3V_2O_5$ to α-V_2O_5 reversibility is extremely challenging given the large structural rearrangements required. This phenomenon has only been seen before in a very limited number of studies, mostly employing nanosized V_2O_5 materials and never before with electrodeposited material.

Introduction

Improvements in lithium-ion based rechargeable batteries are essential for new technological developments and low-carbon energy technologies.[1] Faster charge/discharge times, better

[a]*Department of Chemistry, University of Warwick, Coventry, CV4 7AL, UK. E-mail: j.macpherson@warwick.ac.uk; Haytham.hussein@warwick.ac.uk; Fax: +44 (0)2476 524112; Tel: +44 (0)2476 573886*

[b]*Department of Physics, University of Warwick, Coventry, CV4 7AL, UK. E-mail: R.Beanland@warwick.ac.uk; Tel: +44 (0)24765 73884*

† Electronic supplementary information (ESI) available: Additional information and figures contains; Experimental set-up for vanadium oxide electrodeposition and Li intercalation using the BDD-TEM electrode, illustration of the *in situ* TEM heating set-up, Chronoamperometric response of vanadium sulphate solution using the BDD electrode in a water-DMF mixed solvent, *in situ* TEM thermal annealing of V_2O_5 from amorphous to crystalline, statistical analysis of the V_2O_5 NBs dimensions and size, XPS survey spectrum of the crystalline V_2O_5 NBs electrodeposited on BDD, unknown vanadium oxide polymorphs, the crystalline structure of α-V_2O_5, electron dose and additional observations of VO surface layers, CV data of the first discharge/charge cycle in a solution of 1 M LiCl, XPS and XRD of the V_2O_5 structure post Li intercalation (Li insertion), XPS and XRD of the V_2O_5 structure post Li deintercalation (Li removal), electrochemical response during the second discharge and charge cycle and the formation of ordered $Li_3V_2O_5$ structure. Low magnification STEM images of V_2O_5 structures after lithiation and delithiation cycles, and references. See DOI: 10.1039/d1ta10208g

capacity retention, and recycling are all under investigation, both in incumbent and new materials technologies.[2-4] Energy density is currently limited by the capacity of the cathode material[5] and in this regard, vanadium pentoxide (V_2O_5) is an interesting candidate as it can achieve a theoretical capacity of ~440 mA h g^{-1} provided three lithium ions (Li^+) can be intercalated reversibly per unit cell.[5] A recent study by Liu *et al.* suggested that the capacity could be even higher due to incorporation of more than three Li^+.[6] The use of such materials is thus an attractive replacement for existing, lower capacity cathodes such as $LiCoO_2$ (~240 mA h g^{-1}) and $LiNi_xCo_y$-$Mn_{1-x-y}O_2$ (~280 mA h g^{-1}).[7] Progress in this field requires an atomic-scale understanding of cathode structural changes that occur during Li^+ ion intercalation and de-intercalation. Furthermore, defining the sites that act as either host(s) for ion insertion and extraction, or facilitate the process, can be crucial to optimising performance of the material.[8]

The ability of vanadium to exist in oxidation states from V^{2+} to V^{5+} results in many stable V–O phases and polymorphs.[9,10] The fully oxidised V^{5+} crystalline form, V_2O_5, has a layered crystal structure that allows rapid intercalation of Li^+ and other suitably sized ions such as Zn^{2+}, Mg^{2+}, Al^{3+} *etc.*,[11-13] which has made it a material of interest in Li^+ and metal-ion battery cathode technology for some time.[14-18] The performance of V_2O_5

This journal is © The Royal Society of Chemistry 2022

J. Mater. Chem. A, 2022, **10**, 8515–8527 | 8515

as a cathode material is strongly dependent on crystal size, with Li^+ apparent diffusion coefficients, and hence charge/discharge times, increasing by over five orders of magnitude as the crystal size drops below 100 nm.[16,18–21] V_2O_5 nanostructures have been produced *via* a variety of synthetic methods including hydrothermal/solvothermal, electrospinning, wet-chemical, sol–gel, polyol, atomic layer deposition, and chemical vapor deposition (CVD).[6,22–27] Whilst little used for V_2O_5 synthesis,[19,21,27] electrodeposition has the inherent advantage that the material is, by virtue of the deposition process, electrically contacted to the electrode surface. This is an advantage over other methods which often require further processing, *e.g.* the use of binders and conductive polymer pastes[28] to form an electrical contact and improve the adhesion of the particles to the collector surface.

During Li^+ intercalation, bulk crystalline V_2O_5 undergoes a sequence of transformations with the phases $\alpha \to \varepsilon \to \delta \to \gamma \to \omega$, each accommodating an increasing number of intercalated ions.[29,30] In the absence of Li^+, the starting, α-phase V_2O_5 is comprised of chains of edge-sharing square-based pyramids in which each V is bonded to five O atoms.[30] Adjacent chains form sheets held together by van der Waals forces, between which Li^+ ions are readily intercalated.[31,32] Progressive Li^+ intercalation induces increasing buckling in the sheets to form the ε, δ and γ phases.[31] In contrast, the ω-phase is very different; the square-based pyramids convert to VO_6 and LiO_6 octahedra in a disordered rock-salt structure.[29,33] In bulk material, this transformation is relatively slow and subsequent delithiation does not result in complete removal of Li^+ and restoration of the α-phase.[14] Instead, a disordered rock-salt or amorphous material is formed.[6,33]

An intriguing observation made by several research groups is that the α to ω phase transformation during Li intercalation/deintercalation can be made *reversible*, by employing V_2O_5 nanostructures.[14,17,30,34] These studies indicate that the dimensions of the nanostructure play a crucial role in achieving reversibility.[17,35] For example, a recent *in situ* transmission electron microscopy (TEM) observation of current-driven lithiation of V_2O_5 nanowires (5–15 nm in thickness and 20–60 nm in width), grown by hydrothermal synthesis, showed a reversible $\alpha \to \omega \to \alpha$ transformation,[34] over one cycle. This study also reported formation of an amorphous surface layer $\sim$2 nm thick on the crystalline V_2O_5 after one cycle.[34] Earlier work using TEM with V_2O_5 nanowires, grown by CVD, also observed single-cycle reversibility (with insertion and removal of Li^+ chemically driven), although no information was given on the specific nanowire dimensions.[17] In contrast, a complementary *in situ* TEM study also employing V_2O_5 nanowires, grown by hydrothermal synthesis (50–130 nm in width, no reports on thickness) showed progressive transformation to the intermediate γ-phase only,[36] and no observation of the ω-phase. This study also reported the observation of a Li oxide shell which formed during Li^+ intercalation.[37]

In this work, we first aim to demonstrate that electrically contacted V_2O_5 nanostructures can be produced using electrodeposition procedures, without the use of electrode templates[38] or surfactants.[27] An atom-level understanding of the resulting

crystalline material and its properties in relation to the first electrochemically driven Li^+ discharge/charge process is then obtained using *ex situ* using aberration-corrected scanning TEM (ac-STEM). Complementary electron energy-loss spectroscopy (EELS), X-ray diffraction, and X-ray photoelectron spectroscopy (XPS) measurements are also recorded. Preliminary data on the second cycle of lithiation is also presented.

Experimental

Solutions and chemicals

Vanadium oxide electrodeposition solutions consisted of 0.1 M vanadium(IV) oxide sulfate hydrate ($VOSO_4 \cdot H_2O$, 99%, STREM chemicals, UK) in 0.5 M sulfuric acid (H_2SO_4, 99.99%, Sigma-Aldrich, UK) (pH = 1.87), 15 mM H_2O_2, and 0.3 M $ZnSO_4$ dissolved in Milli-Q water (18.2 MΩ cm, Millipore Corp., U.S.) and *N,N*-dimethylformamide (DMF, Sigma-Aldrich, UK) at 20 °C. The ratio of water to DMF was 3 : 1. All chemicals were used as received without further purification. For all experiments, the solutions were left aerated.

Materials and electrode fabrication

Polycrystalline 5 × 10 mm BDD, 80 μm thick, with a boron dopant level of $\sim$3 × 10^{20} B atoms per cm^3 was used as the starting material for production of the BDD TEM substrates (cut to a disk diameter = 3 mm, using laser micromachining).[39,40] The BDD was grown using microwave CVD by Element Six (Harwell, Oxford, UK) and both surfaces were mechanically polished to $\sim$ nm surface roughness. The fabrication procedure for the production of the BDD-TEM substrates is described in ref. 41. For electrochemical characterisation, BDD material of the same dopant density but 200 μm thick and polished to the same surface finish (on the growth surface only) was employed. A Ti/Au ohmic contact was made to the BDD electrode as previously described.[39,41] The geometry of the electrode area exposed to solution was defined using adhesive Kapton tape, which contained a laser-micromachined circular hole, 5 mm in diameter. The back face was also insulated using adhesive Kapton tape to prevent solution access. The electrode surface was cleaned by first polishing with alumina powder (0.05 μm particles, micropolish, Buehler, Germany) and then further polished on a water-saturated polishing pad (micropolish, Buehler, Germany). The electrode was then cycled in 0.5 M HCl for 5 minutes to verify a clean surface *via* the cyclic voltammetric (CV) response *i.e.* CV cycles which are reproducible with a low background current. The electrode surface was further imaged using optical microscopy (Leica DM4000M upright microscope) and the scanning electron microscopy (SEM: Zeiss Gemini) to confirm the surface was clean.

Electrochemical synthesis of vanadium oxide nanobelts using pulse-reverse anodic electrodeposition

V_2O_5 nanobelt synthesis was achieved using an electrochemical potential pulse (chronoamperometry) methodology in a mixed water–DMF solution containing 0.1 M $VOSO_4 \cdot H_2O$.[42–44] First (i) a cathodic potential was applied −0.35 V *vs.* SCE for 50 s, then

8516 | *J. Mater. Chem. A*, 2022, **10**, 8515–8527

This journal is © The Royal Society of Chemistry 2022

(ii) +1 V *vs.* SCE for 5 s then (iii) +2 V *vs.* SCE for 50 s, then (iv) +1.5 V *vs.* SCE for 100 s followed by (v) +2 V *vs.* SCE for 50 s. All five steps are referred to as a "potential pulse sequence". The rationale behind the pulse potentials chosen is described in the results and discussion section. For the majority of experiments one potential pulse sequence was carried out unless otherwise stated in the text. After electrodeposition, the electrodes were gently rinsed in deionized water for 60 s. The electrodes were stored in a vacuum desiccator for 1 hour before being annealed in a tube furnace under an air atmosphere for 2 h at 350 °C to crystallise the V_2O_5 (*vide infra*) The loading mass of the V_2O_5 on the BDD electrode was measured to be $\sim 1.84 \times 10^{-3}$ g cm^{-2}, and assumed consistent between different electrode geometries by keeping the charge passed constant ($=0.097$C) for each electrodeposition. The mass of deposit was measured using a Metrohm precision microbalance with an accuracy of 0.1 µg.

Electrochemical measurements

All electrochemical experiments were carried out using a three-electrode set-up controlled by a potentiostat (Metrohm Autolab PGSTAT128N and CompactStat Ivium Technologies, Netherlands) using a dipped electrode arrangement (5 mm diameter electrode or the BDD-TEM electrode set-up).[41,45–47] A commercial SCE attached to a luggin capillary filled with the electrolyte solution was used as the reference electrode, a helical Pt wire served as the counter electrode, and BDD, in either the BDD disk electrode or BDD-TEM electrode configuration, was employed as the working electrode. The electrochemically deposited and thermally annealed V_2O_5 on BDD was used for the Li$^+$ ion intercalation/deintercalation studies. The electrochemical performance of the V_2O_5-BDD electrodes was assessed in a three-electrode electrochemical cell using CV and galvanostatic discharge–charge curves. Both were recorded in a mixed water–acetonitrile (MeCN) (1 : 3) electrolyte containing 1 M LiCl and 1 M LiClO$_4$, the latter using a potential window of 1.5–3.6 V *vs.* Li|Li$^+$ with an applied current of 0.00572 mA (active mass $= 1.3 \times 10^{-4}$ g) over a period of 10 hours discharge (-0.00572 mA) and 10 hours charge ($+0.00572$ mA). This corresponds to a C/10 current rate with respect to 3Li$^+$ per V_2O_5 and rated capacity of 440 mA h g^{-1}. The mixed solvent electrolyte was used to widen the electrochemical stability window.[48] Additionally, since MeCN is characterised by a low viscosity and can readily solvate Li$^+$,[49–51] Li$^+$ diffusion through the V_2O_5 material is promoted,[47] resulting in improved capacity and cyclability.[52]

Scanning transmission electron microscopy tracking of Li intercalation behaviour and *in situ* TEM heating study

To study Li$^+$ ion intercalation/deintercalation at the atomic scale, V_2O_5 was electrodeposited directly onto the BDD TEM disk electrodes, which decrease in thickness from the edge of the disk to a hole at the centre ~ 100 µm in diameter.[41] The region up to ~ 30 µm from the edge of the hole is electron transparent. The BDD TEM electrode was electrically connected using a fine metal clamp attached to the BDD Ti/Au contact and dipped into the appropriate electrolyte solution using a manual

x,y,z micropositioner (Newport, Oxford, UK) such that the central hole was in the solution but the Ti/Au contact remained dry. The setup is shown in ESI1, Fig. S1.† Prior to STEM imaging the BDD TEM electrode was stored under vacuum at 50 °C for 6 h in order to ensure the surface remained clean and free of contamination.

For TEM evaluation of the high temperature annealing process, the BDD TEM electrode was mounted in a Gatan 652 double tilt heating holder and selected area electron diffraction (SAED) patterns were collected from a region of the V_2O_5 as the temperature was slowly increased at a rate of 3.18 °C min^{-1} to 380 °C under vacuum (ESI2, Fig. S2†).

Surface characterisation and TEM

Field emission (FE) SEM was used to obtain low magnification images of the V_2O_5 NBs after electrochemical deposition. FE-SEM images were recorded using an in-lens secondary electron detector on a Zeiss Gemini operating at 2 kV. Higher resolution images were recorded using a JEOL-JEM 2100 (LaB$_6$) microscope operated at 200 kV. The impact of Li intercalation/de-intercalation on the shape, structure, size, chemical composition, and evolution of the V_2O_5 NBs was investigated using ac-STEM in a double aberration-corrected JEOL JEM-ARM200F TEM/STEM, operating at 200 kV equipped with a Gatan Quantum EELS. Annular dark field (ADF)-STEM and bright field (BF)-STEM images were recorded simultaneously with a probe current of 23 pA and a convergence semi-angle of ~ 16 mrad. The inner collection semi-angle for ADF-STEM imaging was 38 mrad. Since V_2O_5 is known to be electron beam sensitive[53] great care was taken to minimise electron dose. Crystals already aligned to the incident beam were imaged. To confirm the chemical nature of the V_2O_5, EELS spectra were recorded, at a probe convergence semi-angle of 32 mrad, a spectrometer collection semi-angle of 25 mrad and a dispersion of 0.1 eV per channel. The energy resolution of the EELS measurements was 1.2 eV, estimated from the full-width-half-maximum of the zero-loss peaks. For statistical analysis, $n = 150$ V_2O_5 NBs were analysed in terms of length and width, from three different regions of a BDD TEM electrode.

Phase identification of the BDD-V_2O_5 electrodes prior to and after lithiation were investigated using grazing incidence X-ray diffraction (XRD; Malvern Panalytical Empyrean 3 with multicore optics (iCore/dCore), giving Cu K$_a$ radiation). The incident beam was narrowed using a 1/16° slit to minimise beam spread at low angle. A parallel plate collimator with a solid state Pixel 3D detector operating as a point detector (0D) mode was used with a step size of 0.03° 2q. Prior to measurement, the sample surface was adjusted so that it was flat and cut the direct X-ray beam in half, assuring that the sample was in the centre of rotation of the goniometer. An incident angle of 2° was used. The grazing incidence XRD data were analysed using the Panalytical HighScore Plus software (v4.8) and the peaks matched against reference patterns from the latest ICDD database. To aid the pattern matching, the elements were restricted to just V, H, O. The diamond peaks were also accounted for.
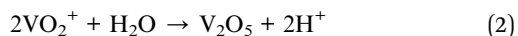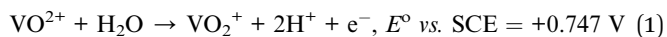
This journal is © The Royal Society of Chemistry 2022

J. Mater. Chem. A, 2022, **10**, 8515–8527 | 8517

X-ray photoelectron spectroscopy (XPS) was conducted using a Kratos Analytical Axis Ultra DLD spectrometer with a monochromated Al Kα X-ray source (1486.69 eV) operated at 156 W in a chamber with a base pressure below 1×10^{-10} mbar. Samples were mounted on the sample bar using electrically conductive carbon tape to ensure conductivity between the sample surface and ground, thus eliminating surface charging. Survey spectra were collected using an analyzer pass energy of 160 eV at 1 eV increments, each of which were integrated for 200 ms. High resolution core level spectra were collected using a pass energy of 20 eV (resolution of approximately 0.4 eV) using multiple sweeps in order to improve the signal-to-noise ratio. Data were analysed using the CasaXPS package, employing mixed Gaussian–Lorentzian (Voigt) lineshapes and Shirley backgrounds. The transmission function and work function of the spectrometer were calibrated using clean polycrystalline Ag foil.

For XRD and XPS, the electrochemical potential pulse sequence was repeated five times to ensure sufficient deposit on the electrode surface such that measurable signals could be obtained.

Results and discussion

Electrochemical fabrication and characterisation of high aspect ratio V₂O₅ NBs

V_2O_5 nanostructures were synthesised using a five-step potential pulse sequence in a mixed water (acidified) – DMF solvent system containing vanadium sulfate ($VOSO_4$). Thermodynamically, electrodeposition of V_2O_5 from acidic aqueous media is possible *via* an electrochemical (E), chemical (C)[54] mechanism, as shown in eqn (1) and (2) for pH < 2:

$$VO^{2+} + H_2O \rightarrow VO_2^+ + 2H^+ + e^-, E^\circ \text{ vs. SCE} = +0.747 \text{ V} \quad (1)$$

$$2VO_2^+ + H_2O \rightarrow V_2O_5 + 2H^+ \quad (2)$$

However, experimentally the process is complicated by electrochemical oxidation of water overlapping with $[VO]^{2+}$ oxidation on most electrodes.[38,44,54–56] Furthermore, accumulation of protons locally (eqn (1)) during electrochemical oxidation results in a further decrease in local pH at the electrode surface and re-dissolution of the deposited material becomes a possibility.[38,44,54–56] Conversely, at pH values above 3.5, VO_2 will precipitate according to:[38,44,54–56]

$$VO^{2+} + H_2O \rightarrow VO_2 + 2H^+ \quad (3)$$
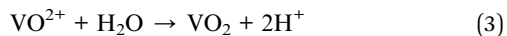
Hence there is only a very limited pH window over which V_2O_5 electrodeposition can be successfully achieved, as also shown by the Pourbaix diagram.[38]

To circumvent this problem, we use a dual approach, (i) the use of BDD electrodes which, due to the catalytic inertness of the surface, kinetically retard water oxidation[39] and (ii) a mixed solvent media, here H_2O (pH = 1.87) and DMF, where DMF is added to the water in a ratio of (water : DMF) 3 : 1. Mixed solvents systems are useful in electrochemical systems as they alter the properties of the individual solvent. Here we use this to effect by adding the polar solvent DMF to help further increase the electrolyte/solvent window.[57,58] DMF has a similar dielectric constant and is miscible with water and thus also favours dissolution of inorganic compounds,[59] such as VO^{2+}, but is more viscous. It also plays a role in controlling the morphology of the resulting deposit, as has been shown in the literature for other mixed solvent electrodeposition systems.[60,61]

The electrochemical signature of $[VO]^{2+}$ in a water (pH = 1.87) : DMF (3 : 1) solution was first assessed using CV at the 5 mm diameter BDD disk electrode, as shown in Fig. 1, starting at 0.00 V (*vs.* SCE) and scanning positive to +2.00 V, and then negative to −2.00 V *vs.* SCE. In Fig. 1a–d, one oxidation peak, at $E_p = +1.40$ V, due to the oxidation of V^{4+} (*i.e.* VO^{2+}) to V^{5+} (*i.e.* V_2O_5) is observed (Ox1), free from any interference from water oxidation, which occurs at >2 V during the first scan (Fig. 1a). Upon reversing the scan direction, two reduction peaks are observed ($E_p = +0.3$ V and −1.5 V). At $E_p = +0.30$ V, R1 corresponds to stripping of the electrodeposited V_2O_5 (V_2O_5 to VO_2^+) followed by reduction of VO^{2+} to V^{3+},[44] at $E_p = -1.50$ V (R2). The generation of a new species, V^{3+}, is evident during the second cycle, where a second oxidation peak is now observed (Fig. 1b), at $E_p = +0.55$ V (Ox2). This is most likely due to oxidation of V^{3+} to V^{4+}.[44] Starting from scan 3, all CV scans (scans 3, 4, 5, and 6) are similar to scan 2.

Electrodeposition (ESI3, Fig. S3†) was carried out using a series of five potential pulses. The potential was first held under no current flow conditions (−0.35 V *vs.* SCE). It was then biased at a value just into the start of the VO^{2+} wave in Fig. 1 (+1.00 V *vs.* SCE for 5 s) in order to form V_2O_5 nuclei (eqn (1) and (2)) on the surface which can act as seeds for further nucleation and growth. By then driving the potential significantly more positive in the second oxidation step, the aim was to stimulate fast growth at these isolated centres (+2.00 V *vs.* SCE for 50 s). By modulating between two high positive potentials of +1.50 V *vs.* SCE for 100 s and +2.00 V for 50 s, continuous growth of the nuclei centres whilst enhancing lateral growth, was observed.

The as-deposited material exhibited no crystallinity, as evidenced by SAED, see Fig. 2a. Previous literature suggests crystalline material has a better electrical connection to an underlying electrode support.[22] To crystallise the V_2O_5, thermal annealing in air was employed. Identification of the crystallisation temperature was carried out using an *in situ* annealing SAED study employing a TEM heating holder, and heating from room temperature up to 380 °C, at a rate of 3.18 °C min⁻¹. The full sequence of the twenty-three recorded images is shown in ESI4, Fig. S4.† The first evidence of V_2O_5 crystallisation was the formation of weak intensity peaks in the SAED pattern at 350 °C (Fig. 2b); blue circles mark 111 spots from the BDD substrate. At ∼365 °C the clearly defined spot pattern corresponds to the *d*-spacings of α-V_2O_5, Fig. 2c. The change in appearance of the deposit during annealing is apparent in Fig. 2d (as-deposited) and Fig. 2e (crystallised). These figures also indicate the approximate position of the selected area aperture used to collect the SAED patterns. The very high thermal conductivity[39] of the BDD-TEM substrate means that the temperature of the BDD electrode will be extremely close to the temperature of the micro furnace of the TEM holder.[62]

8518 | *J. Mater. Chem. A*, 2022, **10**, 8515–8527

This journal is © The Royal Society of Chemistry 2022

Using the *in situ* TEM study to guide controlled crystallisation of electrodeposited V_2O_5 on the BDD electrode, all subsequent studies used a 2 h anneal in air at 350 °C followed by an extended cool-down from 350 °C to room temperature (12 hours) prior to further analysis. The resulting material was analysed using STEM, XPS, and powder XRD. ADF- and BF-STEM images of thermally annealed V_2O_5 on a BDD TEM substrate are displayed in Fig. 3a and b and show a dense mat of NBs (acicular crystals); see also ESI5, Fig. S5 and Table S1† for a statistical analysis of crystal size dimensions. Surface sensitive XPS of the annealed material on a BDD-TEM substrate was consistent with formation of α-V_2O_5 (see also ESI6, Fig. S6† for the survey spectrum). The curve-fitted XPS spectrum in Fig. 3c shows an oxygen 1s peak attributed to the V–O stretch bond at 529.27 eV and vanadium peaks $2p_{1/2}$ at 524.57 eV and $2p_{3/2}$ at 517.15 eV. The main V $2p_{3/2}$ core peak corresponds to a valence state of V^{5+} (solid red fitted curve), associated with V_2O_5, as does $Vp_{1/2}$, whilst the tiny shoulder on the right indicates the presence of a very small amount of V^{4+} (solid orange fitted curve).[18] A small V^{4+} peak has been seen before in the XPS spectra for V_2O_5 material subject to thermal treatment in air at similar temperatures (400 °C).[27,63] XRD of an annealed thick film also confirms

crystallisation (Fig. 3d). The ω-2θ plot exhibits peaks at 21°, 27°, 32°, and 34° corresponding to the crystal planes (101), (110), (400), (211) of α-V_2O_5 (ICDD 00-041-1426, *Pmmn*, $a = 11.519$ Å, $b = 3.563$ Å, $c = 4.375$ Å). The strong peak at 43° is from the BDD substrate.

To explore the electrodeposited and annealed α-V_2O_5 in more detail, Fig. 4 shows high resolution aberration-corrected ADF-STEM images. In Fig. 4a the characteristic parallelepiped acicular shapes (also referred to as 'calissons'[20]) of the V_2O_5 NBs are again evident. By taking side-on views of the NBs (*e.g.* Fig. 4b showing a [100] view and the (001) facets), it was possible to determine thickness values. These were found to be typically in the range 10–20 nm. The long axis of the NBs lies parallel to [010] and the NBs had a mean length of 134 nm (range 15–221 nm) and mean width 9 nm (range 5–37 nm), SI5.† Occasionally other unidentified polymorphs were observed (see ESI7, Fig. S7†).

More detailed information on atom arrangement in a NB is shown in Fig. 4c. Focusing on the region away from the edge first, the ADF-STEM image, where only the high atomic number V atoms produce contrast, confirms the material is α-V_2O_5. A schematic of the structure is shown at the top and left of
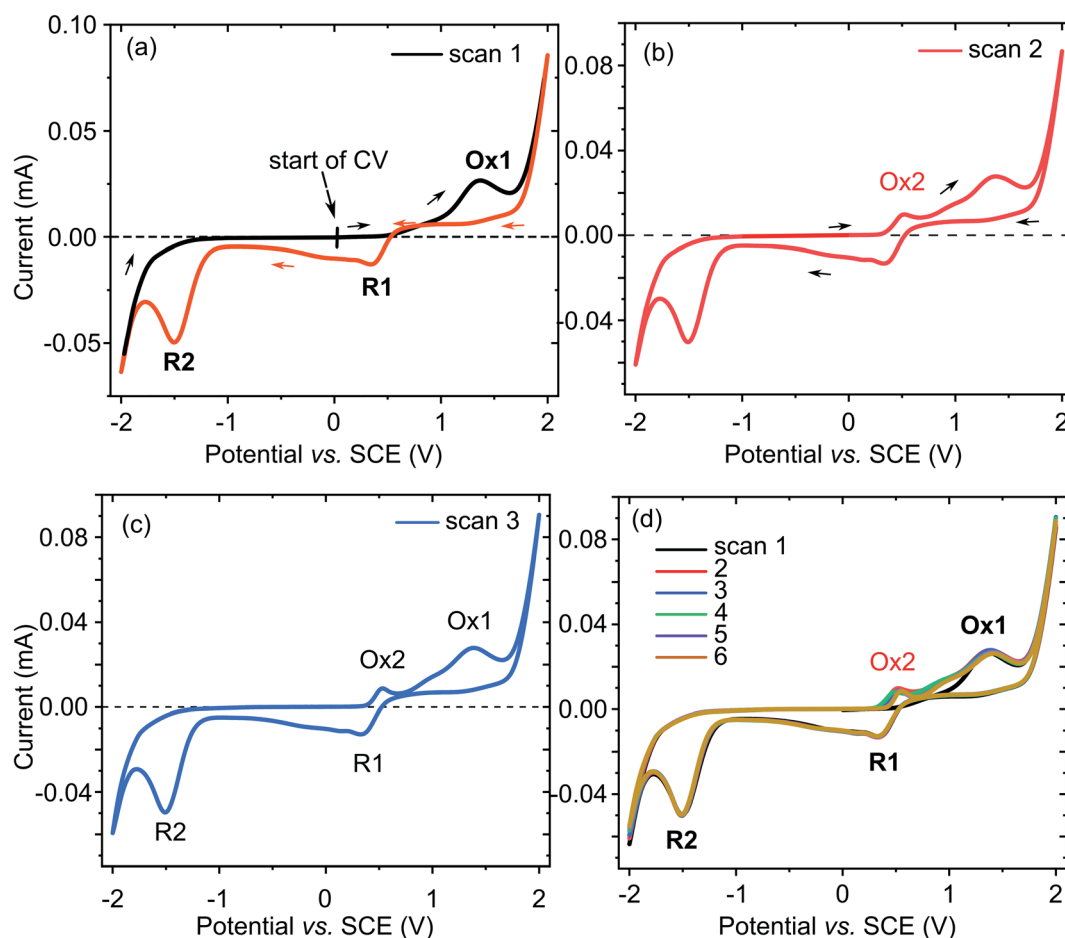

Fig. 1 CV of the electrochemical behaviour of $VOSO_4$ in water : DMF (3 : 1) mixed solvent. (a) First scan indicating the starting potential and the direction of the scan sweep, scanning anodically first, (b) is the second scan, and (c) is the third scan. (d) Repetitive cycling where 6 scans were recorded at 0.1 V s^{-1}.
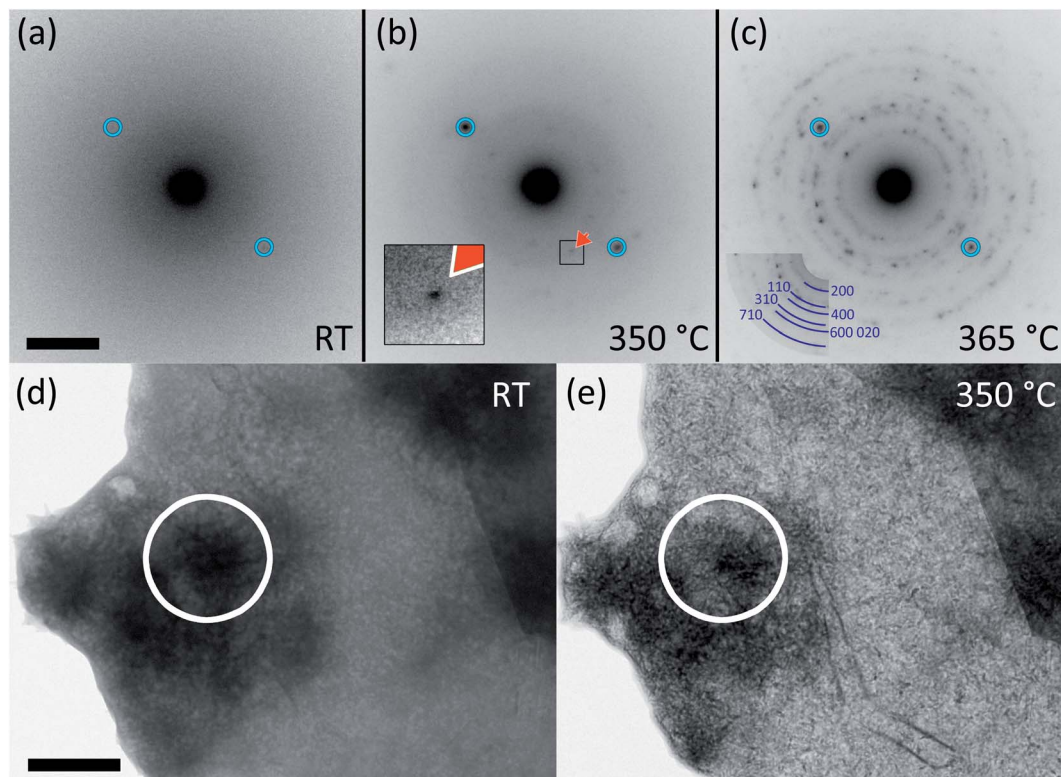
Fig. 2 *In situ* SAED heating study of the transformation of V_2O_5 from amorphous to crystalline during temperature–controlled annealing. (a) As-electrodeposited amorphous V_2O_5, at room temperature, showing only diffuse contrast (scale bar is 10 nm^{-1}). (b) The first appearance of crystalline V_2O_5 spots at 350 °C, one of which is marked by an arrow and enlarged with contrast enhanced in the inset. (c) Rings of spots, showing full conversion to crystalline material at 365 °C. Blue circles mark 111 spots from the BDD TEM support; the visibility of these spots changed during the experiment, possibly due to buckling of the thin specimen as it was heated. (d) and (e) images corresponding to (a) and (b) with the position of the SA aperture marked. Scale bar is 500 nm.

Fig. 4d, where V–O polyhedra are shown in orange, individual V atoms are represented by orange circles and O atoms are represented by blue circles. α-V_2O_5 consists of (001) sheets, comprised of [010] chains of edge-sharing square-based pyramids in which each V lies close to the base and is bonded to five O atoms. For each pyramid there is an sixth oxygen atom present but it is slightly too distant to form the appropriate bond for an octahedral geometry.[30,64]

In the (001) schematic of α-V_2O_5 of Fig. 4d, half of the pyramids point down towards [00$\bar{1}$], (marked '*a*'; the flat base of the pyramid is visible), and half point upwards towards [001], (marked '*b*'; apex and facets of the pyramid are visible). The horizontal [010] chains of pyramids have apices that alternate in an up-up-down-down *b*–*b*–*a*–*a* sequence. As the *a*–*b* chains connect at pyramid corners, there is also a row of empty sites, marked '*c*' in Fig. 4d. This *a*–*b*–*c*, filled-filled-vacant stacking sequence is evident in the ADF-STEM images in Fig. 4c and d. The two rows of pyramids with central V^{5+} atoms can be seen with bright contrast, while the third, empty, row is much darker in comparison. A multislice simulation of the ideal α-V_2O_5 structure is also shown on the left of Fig. 4d connecting the atomic model to the experimental image and as an overlay in Fig. 4c. Further information on the crystal structure of α-V_2O_5 and BF-STEM images are given in ESI8, Fig. S8 and S9.†

Fig. 4c, and at higher resolution in Fig. 4d, also shows the presence of a change in structure at the edge of a (010) facet, noting it was not possible to resolve this feature on all facets of a NB or indeed on all NBs. The atom arrangement appears consistent with a rock-salt type structure, VO, where V is now octahedrally coordinated to six O atoms, forming a structure of close-packed edge-sharing octahedra as shown in the top and right schematics in Fig. 4d. Rock-salt VO can be produced in bulk form,[65] with a range of stoichiometry VO$_x$ (0.8 < *x* < 1.3) and high concentrations of both V and O vacancies.[66] As is apparent from Fig. 4d, the [010] rows of atoms are continuous throughout the NB, but in the VO region there is no row of empty sites and the [001] view shows a square array of bright atom columns. This image is in excellent agreement with the multislice simulation that bridges the gap between the structural model and experimental image on the right of Fig. 4d. The VO structure often appears noticeably brighter than the bulk of the crystal (see also ESI9, Fig. S10†), which is also consistent with the higher density of oxygen-depleted VO, in comparison with α-V_2O_5. From Fig. 4d information on the lattice mismatch between VO and α-V_2O_5 along [100] can also be obtained; the plane spacing of V_2O_5 is 11.512 Å while that of VO is 4.075 Å, giving a 3 : 1 matching with a misfit of 6%. However, despite the difference in crystal structure the VO region appears coherent
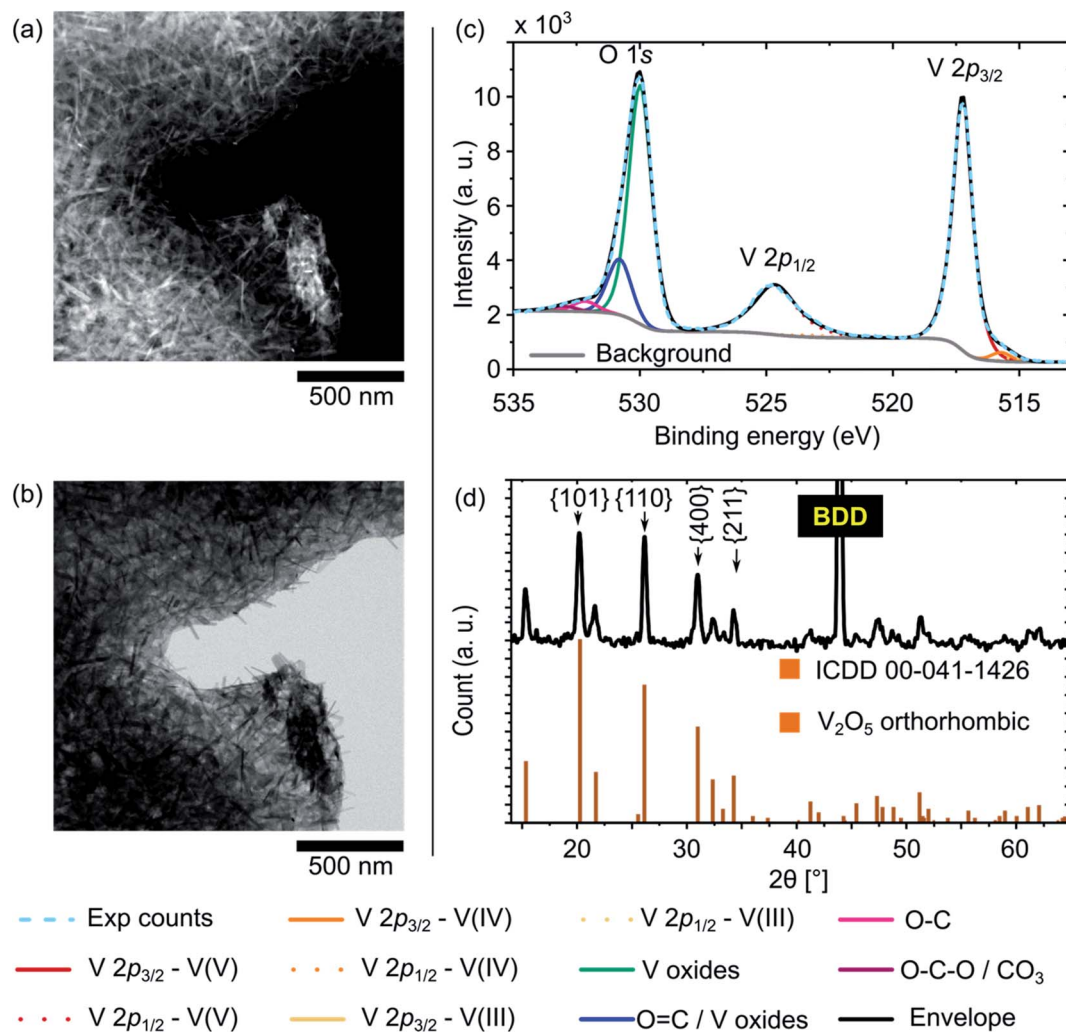
8520 | *J. Mater. Chem. A*, 2022, **10**, 8515–8527

This journal is © The Royal Society of Chemistry 2022

Fig. 3 Morphology and analysis of electrodeposited and thermally annealed V_2O_5. (a and b) ADF-STEM and BF-STEM images of high coverage V_2O_5 on a BDD TEM support, forming a dense mat of acicular crystals. (c) XPS spectrum and curve fitting of the O 1s and V $2p_{3/2}$ peaks. (d) ω-2θ XRD pattern identifying the deposit as the orthorhombic V_2O_5 structure.

with the α-V_2O_5 crystal, with an orientation relationship $[100]_{VO}//[100]_{V_2O_5}$, $[001]_{VO}//[001]_{V_2O_5}$. Other examples of VO formation on a NB edge are given in ESI9, Fig. S10.†

It is interesting to compare the macroscale (XRD and XPS) with the atom scale (ac-STEM and EELS) data in Fig. 3 and 4. XRD which is a bulk measurement indicates the formation of α-V_2O_5 crystals. XPS which is sensitive to only the first few surface layers[38] confirms this, *via* observation of a dominant V^{5+} oxidation peak, but also indicates the presence of a small amount of V^{4+} but no V^{2+}(as expected for VO). For crystals subject to thermal annealing, under both UHV (thermal reduction) and in air, loss of oxygen and the formation of V^{4+} oxidation states has been previously documented, using XPS, EELS and DFT,[27,64,67] with DFT predicting loss of vanadyl oxygens and formation of a V–O–V bond between layers upon thermal reduction.[64,68] However, given that XPS does not show a V^{2+} signature, VO presence must be at levels below the detection sensitivity of XPS in the area of the XPS measurement.

This fits in with our TEM observations that the VO layer is not present on all NBs imaged or indeed all facets.

It is also important at this stage in the discussion to consider the possible effect of the electron beam on the ac-STEM data. In previous high resolution TEM studies, α-V_2O_5 subject to high doses of electron irradiation in UHV for long periods of time (minutes to tens of minutes), resulted in a transition to rock-salt VO.[53,69,70] By lowering the flux of electrons it was possible to observe the intermediate phases V_4O_6 and V_6O_{13} before reaching VO.[53] However, in our study, the radiation dose in our work is approximately three orders of magnitudes smaller than previous work, and imaging was for much shorter periods of time (10 μs per pixel), see ESI9.† When the VO structure was present it was observed immediately and noticeable structural changes in the NBs were only seen after having made several passes over the NB with the electron beam. This suggests that the thermal anneal was responsible for the observed atomic rearrangements.
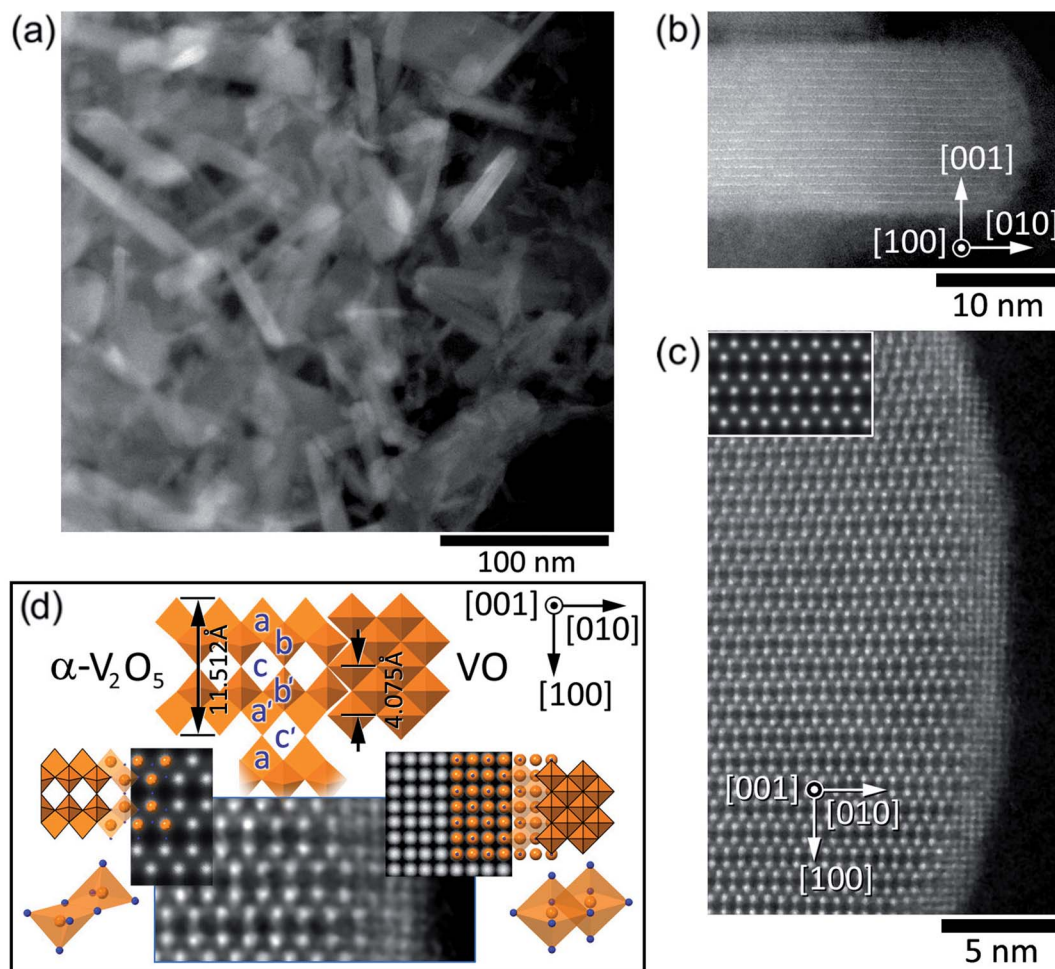
Fig. 4 ADF-STEM of electrodeposited and thermally annealed α-V$_2$O$_5$. (a) Electrodeposited and thermally annealed α-V$_2$O$_5$ on BDD with high coverage, forming a mat of acicular crystals with lengths 15–221 nm. (b) A single α-V$_2$O$_5$ NB seen edge-on, with (001) facets and long axis parallel to [010]. (c) Another NB viewed face-on, close to the [001] axis, showing distinctive double-layers of vanadium (inset: multi-slice simulation of [001] α-V$_2$O$_5$). An altered layer 1–2 nm in thickness is visible at the (010) facet. (d) The altered layer at the (010) facet has an appearance consistent with rock-salt VO, with octahedral coordination of vanadium (orange) to oxygen (blue).

Characterisation of the α-V$_2$O$_5$ NBs during one cycle Li intercalation and deintercalation

The first lithiation (discharge) and de-lithiation (charge) cycle for electrodeposited and annealed α-V$_2$O$_5$ NBs on a BDD electrode was investigated galvanostatically by cycling between +3.6 V and +1.5 V *vs.* Li|Li$^+$ at a C/10 current rate (see experimental section). The discharge–charge curve of the α-V$_2$O$_5$ NBs is presented as a potential (*y* axis) *versus* composition (top axis), represented as a number of intercalated Li (*i.e.* Δ*x*Li in Li$_x$V$_2$O$_5$)/ specific capacity in mA h g^{-1} (bottom axis) and is shown in Fig. 5 for the first discharge (lithiation – left hand side) – charge (delithiation – right hand side) cycle.

During discharge, the electrode is cycled to less positive potential values to promote intercalation/insertion of Li$^+$ ions into the α-V$_2$O$_5$ material (lithiation). Fig. 5a shows a series of distinct potential plateaus, which demonstrate the formation of different Li$_x$V$_2$O$_5$ phases. The galvanostatic profile shows various sloped regions associated with the following sequence of transitions; α → ε → δ → γ → ω, Li$_x$V$_2$O$_5$. The first three transitions describe the Li$_x$V$_2$O$_5$ phases with increasingly puckered layers of VO$_5$ square-based pyramids, as the number of Li$^+$ intercalated per unit cell increases.[30,31,33] The fourth represents the formation of the rock salt ω-Li$_3$V$_2$O$_5$ phase. In a similar manner to the structural transition α-V$_2$O$_5$ → VO, we expect this phase transition to involve conversion of VO$_5$ square-based pyramids to VO$_6$ octahedra. This is accompanied by the expulsion of a fraction of V atoms into unoccupied rows, most likely driven by exchange with Li$^+$, where they also become octahedrally coordinated. Complementary CV data showing the voltammetric response of the NBs during the first discharge/ charge cycle, in a solution of 1 M LiCl + 1 M LiClO$_4$ in 1 : 3 mixture of water and MeCN, is shown in ESI10, Fig. S11.†

A maximum discharge specific capacity of 440 mA h g^{-1} was achieved during the first galvanostatic cycle (on discharge/ lithiation) which is as expected if all the material was converted to ω-Li$_3$V$_2$O$_5$. A number of Li$^+$ per V$_2$O$_5$ (Δ*x*Li) in Li$_x$V$_2$O$_5$ of ~3.0 was also achieved. The lithiated V$_2$O$_5$ material, obtained after discharging, was further investigated by STEM and

8522 | *J. Mater. Chem. A*, 2022, **10**, 8515–8527

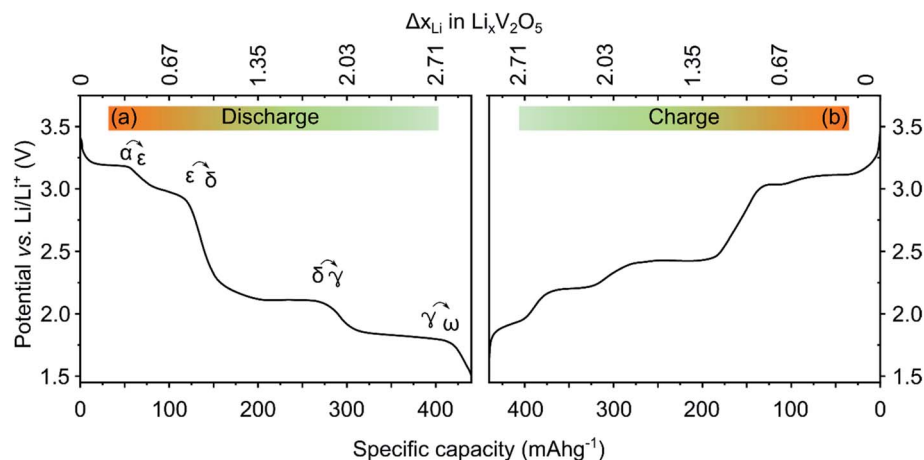This journal is © The Royal Society of Chemistry 2022

Fig. 5 Galvanostatic potential profile. First discharge (left hand side) − charge (right hand side) of α-V_2O_5 NB-BDD electrode in 1 M LiCl + 1 M LiClO$_4$ in 1 : 3 mixture of water and MeCN at C/10 rate.

macroscale XPS and XRD characterisation. The XPS data of the V region is presented in Fig. 6 and the survey spectrum as well as the XPS data of the Li and O regions are shown in ESI11, Fig. S12 and S13.† Curve fitting of the core XPS spectrum in Fig. 6 between 510 eV and 535 eV, and comparison with Fig. 3a, reveals the changes in the valence state of vanadium upon lithiation. In particular, the dominant V 2p$_{3/2}$ peak at ∼517 eV can now be deconvoluted into three peaks; the solid red, orange and yellow fitted curves indicate V^{5+} (517.5 eV), V^{4+} (516 eV) and V^{3+} (∼515.5 eV). The data shows a substantial increase in the $V^{4+/3+}$ valence states compared to the pristine material (Fig. 3a). In addition the XPS signal for lithium (Fig. S13 in ESI11;† between 60 eV and 52 eV) confirms lithium incorporation into the material. The presence of $V^{4+/3+}$ highlights the formation of ω-$Li_3V_2O_5$.[6,33] The XRD ω-2θ plot of the material after the first

discharge (lithiation) is also shown in ESI11, Fig. S14,† and is similar to that previously reported by Delmas *et al.*[29] after one cycle.

To reveal the atomic structure of the resulting lithiated NBs after the first full discharge, STEM images were again recorded. Fig. 7a shows the conversion of the NB to the rock salt ω-$Li_3V_2O_5$ phase. In structure, this appears very similar to the VO region at the (010) edge of the α-V_2O_5 NBs (Fig. 4b–d). In this lithiated material, with a nominal Li_3 : V_2 ratio, we may expect V atoms to be replaced by Li in three out of every five octahedra.[6] There are relatively few octahedra in a crystal of only 10–20 nm thickness. Thus, statistical variations in the V occupancy of individual atom columns should also be readily visible since high atomic number atom columns give a larger contrast than low atomic number ones. This is shown in the bottom half of Fig. 7a and is
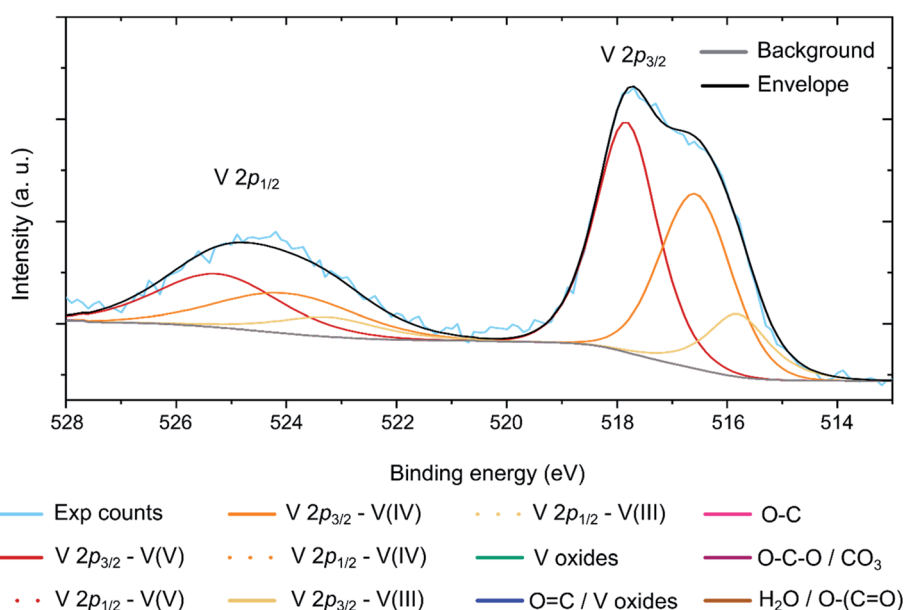

Fig. 6 XPS study of the structure of the V_2O_5 NBs after lithiation (discharge). XPS spectrum and curve fitting of the V 2p of the V_2O_5 NBs after lithiation showing the V 2p$_{3/2}$ and the V 2p$_{1/2}$ regions.

This journal is © The Royal Society of Chemistry 2022

J. Mater. Chem. A, 2022, **10**, 8515–8527 | **8523**

consistent with a mixture of randomly arranged LiO_6 and VO_6 octahedra in the ω phase. This interpretation is also supported by multislice simulations performed using a random structure model overlaid on the images (outlined in green in Fig. 7a). The ω-$Li_3V_2O_5$ structure has the same orientation relationship with respect to the crystal shape as the VO region, but now extends over all of the NB. The lattice parameter of ω-$Li_3V_2O_5$ is 4.095 Å,[6] only slightly larger than that of VO, giving a misfit of 7% to α-V_2O_5. EELS spectrum of the lithiated materials recorded from the centre of the lithiated NB also shows a change in vanadium oxidation state,[36] Fig. 7b (green line). The V $2p_{1/2}$ peak has moved by ∼1.0 eV indicating a V^{3+}/V^{4+} valence state, as expected for formation of ω-$Li_3V_2O_5$,[6,33] and consistent with the XPS data (Fig. 6 and ESI11, Fig. S13†).

The galvanostatic charge profile in Fig. 5b shows several plateaus during the delithiation process at slightly different potential values in comparison with the first discharge process suggesting differences in the dynamics of the mechanism of Li+ intercalation/deintercalation during a single charge–discharge cycle. A maximum charge specific capacity of 439 mA h g^{-1} was achieved, which indicates recovery of the starting material, α-V_2O_5.[1] To further investigate the status of the material after one discharge/charge cycle, ADF-STEM was employed to image individual NBs of the fully charged material (after the first delithiation), Fig. 7c, whilst XPS and XRD measurements were made on the bulk material (ESI12, Fig. S15 and S16†). The ADF-STEM image of a typical NB after the first delithiation process reveals restoration of the original α-V_2O_5 structure but also shows retainment of the thin rock-salt surface layer (VO) (visible at the (010) facets in Fig. 7c, *cf.* Fig. 4c and d). Additionally, EELS spectrum of the delithiated materials recorded from the centre

of the V_2O_5 NB also shows a change in vanadium oxidation state, Fig. 7b (orange line). The V $2p_{1/2}$ peak appears at 519 eV indicating a V^{5+} valence state, as expected for formation of α-V_2O_5. Both the macroscale XPS data (ESI12, Fig. S15†) and XRD (ESI12, Fig. S16†) data are also very similar to the pristine α-V_2O_5 XPS and XRD data recorded in Fig. 3c and d, indicating no remaining lithiated phases and removal of Li+. Finally, whilst the focus of the work was primarily on the first cycle discharge/charge response of electrodeposited α-V_2O_5 we also recorded preliminary STEM experiments and electrochemical data, exploring the second discharge process, shown in Fig. 8 and ESI13, Fig. S17 – S19.†

The second discharge curve shows a similar behaviour to the first discharge profile (ESI13, Fig. S17†), with a discharge capacity of 439 mA h g^{-1} achieved. However, the morphology of the NBs has changed (Fig. 8a, b and ESI13 Fig. S18–S19†), with the crystals becoming more equiaxed and having lower aspect ratios. A high magnification of the crystals after the second lithiation, Fig. 8b, indicates that the cubic ω-$Li_3V_2O_5$ phase is once again obtained and represents the majority of NBs investigated with STEM. The change in morphology is quantified in ESI13, Fig. S20 and S21.† The variable occupancy of the Li/V octahedral sites is again apparent from the variable intensity of the atom columns in Fig. 8b. The multi-slice simulation is shown as an inset. Fig. 8c shows the orientation of the LiO_6/VO_6 octahedra in the [211] view of the lithiated material and correspondence with the simulated disordered ω-$Li_3V_2O_5$. Whilst this observation is interesting, it is clear further investigation is required to understand the impact this morphology change has on the ability of the material to undergo repetitive reversible cycling between α-V_2O_5 and ω-$Li_3V_2O_5$. Furthermore, some

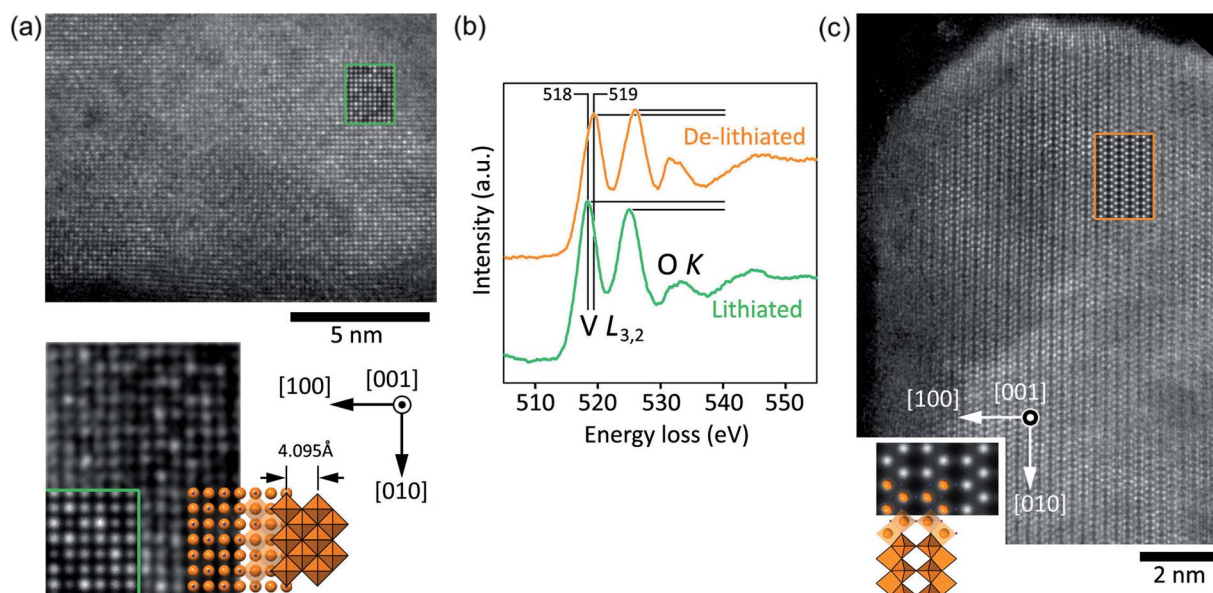**Fig. 7** ADF-STEM of lithiated–delithiated vanadium oxide NBs. (a) After first lithiation, showing the rock-salt ω-$Li_3V_2O_5$ phase. The variable occupancy of the Li/V octahedral site in the rock-salt ω-$Li_3V_2O_5$ phase is apparent from the highly variable intensity of the atom columns in the enlarged ADF-STEM image. Overlays show a multislice simulation of a random disordered rocksalt structure model. (b) Vanadium and oxygen EELS spectra for lithiated and de-lithiated material showing changes in vanadium valence state (see text). (c) After one delithiation, showing reversion to the α-V_2O_5 phase and retainment of the VO surface layer. Multislice simulation shown as an inset.

8524 | *J. Mater. Chem. A*, 2022, **10**, 8515–8527

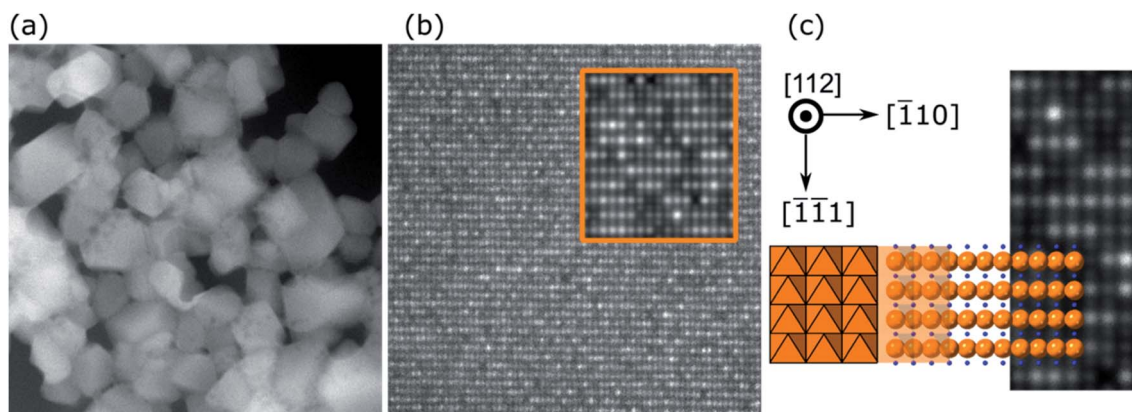This journal is © The Royal Society of Chemistry 2022

Fig. 8 ADF-STEM of vanadium oxide NBs after a second lithiation. (a) Crystal morphologies become noticeably more equiaxed (see also ESI13 Fig. S18†). (b) The material has the rock-salt ω-$Li_3V_2O_5$ phase and as before the variable occupancy of the Li/V octahedral site is apparent from the variable intensity of the atom columns, Multi-slice simulation shown as an inset. (c) Orientation of LiO_6/VO_6 octahedra in this [211] view and correspondence with the simulated disordered ω-$Li_3V_2O_5$ structure.

unidentified ordered structures were occasionally seen (see ESI13, Fig. S19†).

Conclusions

A mixed solvent method, in combination with an electrochemical potential pulse technique, was developed to deposit amorphous V_2O_5 NBs, with thermal treatment used to transform the amorphous V_2O_5 into crystalline α-V_2O_5. The optimal temperature for this process was determined by *in situ* heating TEM. The resulting α-V_2O_5 NBs had thicknesses of 10–20 nm, lengths 15–221 nm (mean 134 nm) and widths 5–37 nm (mean 9 nm). For successful electrodeposition, it was necessary to supress the oxidation of water, achieved through the use of BDD electrodes and a mixed aqueous – aprotic (DMF) solvent, and employ a potential pulse sequence. STEM of the pristine material revealed that the NBs were (in the majority) a single crystal of α-V_2O_5 with a [010] long axis and (100) and (001) faces. A thin surface layer, 1–2 nm in thickness, was found on some NBs in edge regions, with an appearance consistent with a few monolayers of rock-salt VO coherently strained to match the underlying α-V_2O_5 crystal. It was however undetectable in XPS suggesting it was not a significant presence. Further work to understand its significance and origin is underway.

Single cycle charge–discharge data indicated a specific capacity consistent with the reversible incorporation of three Li^+ per unit cell *i.e.* formation of rock-salt ω-$Li_3V_2O_5$. This was confirmed by ac-STEM images of fully lithiated material, which showed not only the rock-salt structure but also variable intensities of atom columns in annular dark field images, indicating a disordered and locally variable composition. Upon full delithiation, α-V_2O_5 was recovered, also evidenced using XPS and XRD, highlighting the one cycle $\alpha \leftrightarrow \omega \leftrightarrow \alpha$ phase reversibility of this nanostructured electrodeposited material. VO surface layers were also again observed in the delithiated material. Preliminary second cycle ac-STEM lithiation studies again revealed formation of the ω phase but interestingly this was accompanied by a morphology change, with the NB crystals

becoming more equiaxed. Further studies are required to establish whether this electrodeposited nanomaterial is a viable battery cathode, when run over many cycles.

Finally, this investigation has demonstrated the importance of STEM as an analysis technique to better understand material transformation in hybrid aqueous/nonaqueous batteries and the potential for using electrodeposition as a synthesis methodology for battery related materials.

Author contributions

HEMH: conceptualization, methodology, data curation, writing – original draft, investigation, writing-review & editing. RB: conceptualization, methodology, investigation, data curation, writing – review & editing & supervision. AS, YH, MW, DW: methodology, investigation, data curation, writing – review & editing. JVM: supervision, conceptualization, methodology, data curation, resources, funding acquisition, investigation, writing – review & editing.

Conflicts of interest

The authors declare no competing financial interest.

Acknowledgements

Notes and references

1 E. Pomerantseva, F. Bonaccorso, X. Feng, Y. Cui and Y. Gogotsi, *Science*, 2019, **366**, eaan8285.

This journal is © The Royal Society of Chemistry 2022

J. Mater. Chem. A, 2022, **10**, 8515–8527 | **8525**

2 K. Kang, Y. S. Meng, J. Breger, C. P. Grey and G. Ceder, *Science*, 2006, **311**, 977–980.

3 C. Liu, Z. G. Neale and G. Cao, *Mater. Today*, 2016, **19**, 109–123.

4 G. Li, T. Ouyang, T. Xiong, Z. Jiang, D. Adekoya, Y. Wu, Y. Huang and M. S. Balogun, *Carbon*, 2021, **174**, 1–9.

5 M. J. Lain, J. Brandon and E. Kendrick, *Batteries*, 2019, **5**, 64–74.

6 H. Liu, Z. Zhu, Q. Yan, S. Yu, X. He, Y. Chen, R. Zhang, L. Ma, T. Liu, M. Li, R. Lin, Y. Chen, Y. Li, X. Xing, Y. Choi, L. Gao, H. S. Cho, K. An, J. Feng, R. Kostecki, K. Amine, T. Wu, J. Lu, H. L. Xin, S. P. Ong and P. Liu, *Nature*, 2020, **585**, 63–67.

7 N. Nitta, F. Wu, J. T. Lee and G. Yushin, *Mater. Today*, 2015, **18**, 252–264.

8 Z. Tu, S. Choudhury, M. J. Zachman, S. Wei, K. Zhang, L. F. Kourkoutis and L. A. Archer, *Nat. Energy*, 2018, **3**, 310–316.

9 J. Stringer, *J. Less-Common Met.*, 1965, **8**, 1–14.

10 Y.-B. Kang, *J. Eur. Ceram. Soc.*, 2012, **32**, 3187–3198.

11 L. Wang, K. W. Huang, J. Chen and J. Zheng, *Sci. Adv.*, 2019, **5**, eaax4279.

12 S. Gu, H. Wang, C. Wu, Y. Bai, H. Li and F. Wu, *Energy Storage Materials*, 2017, **6**, 9–17.

13 H. D. Yoo, J. R. Jokisaari, Y.-S. Yu, B. J. Kwon, L. Hu, S. Kim, S.-D. Han, M. Lopez, S. H. Lapidus, G. M. Nolis, B. J. Ingram, I. Bolotin, S. Ahmed, R. F. Klie, J. T. Vaughey, T. T. Fister and J. Cabana, *ACS Energy Lett.*, 2019, **4**, 1528–1534.

14 C. Delmas, S. Brèthes and M. Ménétrier, *J. Power Sources*, 1991, **34**, 113–118.

15 J. Cocciantelli, M. Ménétrier, C. Delmas, J. P. Doumerc, M. Pouchard, M. Broussely and J. Labat, *Solid State Ionics*, 1995, **78**, 143–150.

16 C. R. Sides and C. R. Martin, *Adv. Mater.*, 2005, **17**, 125–128.

17 C. K. Chan, H. Peng, R. D. Twesten, K. Jarausch, X. F. Zhang and Y. Cui, *Nano Lett.*, 2007, **7**, 490–495.

18 L. R. De Jesus, G. A. Horrocks, Y. Liang, A. Parija, C. Jaye, L. Wangoh, J. Wang, D. A. Fischer, L. F. J. Piper, D. Prendergast and S. Banerjee, *Nat. Commun.*, 2016, **7**, 12022.

19 J.-K. Lee, G.-P. Kim, I. K. Song and S.-H. Baeck, *Electrochem. Commun.*, 2009, **11**, 1571–1574.

20 D. Huo, A. Contreras, B. Laïk, P. Bonnet, K. Guérin, D. Muller-Bouvet, C. Cenac-Morthe, R. Baddour-Hadjean and J. P. Pereira-Ramos, *Electrochim. Acta*, 2017, **245**, 350–360.

21 J. Pu, Z. Shen, C. Zhong, Q. Zhou, J. Liu, J. Zhu and H. Zhang, *Adv. Mater.*, 2019, e1903808, DOI: 10.1002/adma.201903808.

22 Y. Yue and H. Liang, *Adv. Energy Mater.*, 2017, **7**, 1602545.

23 Y. Huang, H. Yang, T. Xiong, D. Adekoya, W. Qiu, Z. Wang, S. Zhang and M. S. Balogun, *Energy Storage Materials*, 2020, **25**, 41–51.

24 S. Zhou, P. Huang, T. Xiong, F. Yang, H. Yang, Y. Huang, D. Li, J. Deng and M.-S. Balogun, *Small*, 2021, **17**, 2100778.

25 E. A. Meulenkamp, W. van Klinken and A. R. Schlatmann, *Solid State Ionics*, 1999, **126**, 235–244.

26 W. Zhong, J. Huang, S. Liang, J. Liu, Y. Li, G. Cai, Y. Jiang and J. Liu, *ACS Energy Lett.*, 2019, **5**, 31–38.

27 Y. Lu and X. Zhou, *Thin Solid Films*, 2018, **660**, 180–185.

28 Y. Lee, *Energies*, 2019, **12**, 658.

29 C. Delmas, H. Cognac-Auradou, J. M. Cocciantelli, M. Ménétrier and J. P. Doumerc, *Solid State Ionics*, 1994, **69**, 257–264.

30 J. Galy, *J. Solid State Chem.*, 1992, **100**, 229–245.

31 P. M. Marley, G. A. Horrocks, K. E. Pelcher and S. Banerjee, *Chem. Commun.*, 2015, **51**, 5181–5198.

32 H. Asayesh-Ardakani, A. Nie, P. M. Marley, Y. Zhu, P. J. Phillips, S. Singh, F. Mashayek, G. Sambandamurthy, K. B. Low, R. F. Klie, S. Banerjee, G. M. Odegard and R. Shahbazian-Yassar, *Nano Lett.*, 2015, **15**, 7179–7188.

33 C. K. Christensen, D. R. Sørensen, J. Hvam and D. B. Ravnsbæk, *Chem. Mater.*, 2019, **31**, 512–520.

34 J. Zhu, H. Shen, X. Shi, F. Yang, X. Hu, W. Zhou, H. Yang and M. Gu, *Anal. Chem.*, 2019, **91**, 11055–11062.

35 A. Mukherjee, N. Sa, P. J. Phillips, A. Burrell, J. Vaughey and R. F. Klie, *Chem. Mater.*, 2017, **29**, 2218–2226.

36 A. Mukherjee, H. A. Ardakani, T. Yi, J. Cabana, R. Shahbazian-Yassar and R. F. Klie, *Appl. Phys. Lett.*, 2017, **110**, 213903.

37 A. Mukherjee, H. Asayesh Ardakani, P. J. Phillips, R. S. Yassar and R. F. Klie, *Microsc. Microanal.*, 2015, **21**, 1819–1820.

38 K. Takahashi, S. J. Limmer, Y. Wang and G. Cao, *J. Phys. Chem. B*, 2004, **108**, 9795–9800.

39 J. V. Macpherson, *Phys. Chem. Chem. Phys.*, 2015, **17**, 2935–2949.

40 L. A. Hutton, J. G. Iacobini, E. Bitziou, R. B. Channon, M. E. Newton and J. V. Macpherson, *Anal. Chem.*, 2013, **85**, 7230–7240.

41 H. E. M. Hussein, R. J. Maurer, H. Amari, J. J. P. Peters, L. Meng, R. Beanland, M. E. Newton and J. V. Macpherson, *ACS Nano*, 2018, **12**, 7388–7396.

42 E. Armstrong, M. O'Sullivan, J. O'Connell, J. D. Holmes and C. O'Dwyer, *J. Electrochem. Soc.*, 2015, **162**, D605–D612.

43 E. Armstrong, D. McNulty, H. Geaney and C. O'Dwyer, *ACS Appl. Mater. Interfaces*, 2015, **7**, 27006–27015.

44 E. Potiron, A. Le Gal La Salle, A. Verbaere, Y. Piffard and D. Guyomard, *Electrochim. Acta*, 1999, **45**, 197–214.

45 H. E. M. Hussein, H. Amari and J. V. Macpherson, *ACS Catal.*, 2017, **7**, 7388–7398.

46 H. E. M. Hussein, A. D. Ray and J. V. Macpherson, *Green Chem.*, 2019, **21**, 4662–4672.

47 H. E. M. Hussein, H. Amari, B. G. Breeze, R. Beanland and J. V. Macpherson, *Nanoscale*, 2020, **12**, 21757–21769.

48 J. Zhu, Y. Xu, Y. Fu, D. Xiao, Y. Li, L. Liu, Y. Wang, Q. Zhang, J. Li and X. Yan, *Small*, 2020, **16**, 1905838.

49 B. G. Cox, G. R. Hedwig, A. J. Parker and D. W. Watts, *Aust. J. Chem.*, 1974, **27**, 477–501.

50 J. S. Loring and W. R. Fawcett, *J. Phys. Chem. A*, 1999, **103**, 3608–3617.

51 M. Shin, H.-L. Wu, B. Narayanan, K. A. See, R. S. Assary, L. Zhu, R. T. Haasch, S. Zhang, Z. Zhang, L. A. Curtiss and A. A. Gewirth, *ACS Appl. Mater. Interfaces*, 2017, **9**, 39357–39370.

52 L. Chen, L. Cao, X. Ji, S. Hou, Q. Li, J. Chen, C. Yang, N. Eidson and C. Wang, *Nat. Commun.*, 2020, **11**, 2638.

8526 | *J. Mater. Chem. A*, 2022, **10**, 8515–8527

This journal is © The Royal Society of Chemistry 2022

53 R. Ai, H. J. Fan and L. D. Marks, *Surf. Sci.*, 1993, **280**, 369–374.

54 D. Rehnlund, M. Valvo, K. Edström and L. Nyholm, *J. Electrochem. Soc.*, 2014, **161**, D515–D521.

55 E. Potiron, A. Le Gal La Salle, S. Sarciaux, Y. Piffard and D. Guyomard, *J. Power Sources*, 1999, **81–82**, 666–669.

56 J.-M. Li, K.-H. Chang and C.-C. Hu, *Electrochim. Acta*, 2010, **55**, 8600–8605.

57 J. C. Hidalgo-Acosta, M. A. Mendez, M. D. Scanlon, H. Vrubel, V. Amstutz, W. Adamiak, M. Opallo and H. H. Girault, *Chem. Sci.*, 2015, **6**, 1761–1769.

58 W. Simka, D. Puszczyk and G. Nawrat, *Electrochim. Acta*, 2009, **54**, 5307–5319.

59 V. Gutmann, *Coordination Chemistry in Non-Aqueous Solutions*, 1968.

60 C. Mele, S. Rondinini, L. D'Urzo, V. Romanello, E. Tondo, A. Minguzzi, A. Vertova and B. Bozzini, *J. Solid State Electrochem.*, 2009, **13**, 1577–1584.

61 K. Maksymiuk, *Electrochim. Acta*, 1993, **38**, 721–727.

62 L. Meng, J. G. Iacobini, M. B. Joseph, J. V. Macpherson and M. E. Newton, *Faraday Discuss.*, 2014, **172**, 421–438.

63 C.-C. Hu, K.-H. Chang, C.-M. Huang and J.-M. Li, *J. Electrochem. Soc.*, 2009, **156**, D485–D489.

64 M. V. Ganduglia-Pirovano, A. Hofmann and J. Sauer, *Surf. Sci. Rep.*, 2007, **62**, 219–270.

65 G. Andersson, *Acta Chem. Scand.*, 1954, **8**, 1599–1606.

66 M. D. Banus, T. B. Reed and A. J. Strauss, *Phys. Rev. B: Solid State*, 1972, **5**, 2775–2784.

67 Q. Wang, H. Wang, Z. Zhou, J. Zuo and C. Zhang, *Nanoscale*, 2020, **12**, 21368–21375.

68 M. V. Ganduglia-Pirovano and J. Sauer, *Phys. Rev. B: Condens. Matter Mater. Phys.*, 2004, **70**, 045422.

69 D. S. Su, M. Wieske, E. Beckmann, A. Blume, G. Mestl and R. Schlögl, *Catal. Lett.*, 2001, **75**, 81–86.

70 H. J. Fan and L. D. Marks, *Ultramicroscopy*, 1989, **31**, 357–364.

This journal is © The Royal Society of Chemistry 2022

J. Mater. Chem. A, 2022, **10**, 8515–8527 | **8527**